Generation of subsurface voids and a nanocrystalline surface layer in femtosecond laser irradiation of a single-crystal Ag target

Chengping Wu, Martin S. Christensen, Juha-Matti Savolainen, Peter Balling, and Leonid V. Zhigilei

Phys. Rev. B **91**, 035413 — Published 12 January 2015

DOI: 10.1103/PhysRevB.91.035413

Generation of sub-surface voids and a nanocrystalline surface layer in femtosecond laser irradiation of a single crystal Ag target

Chengping Wu,[1] Martin S. Christensen,[2] Juha-Matti Savolainen,[2] Peter Balling,[2] and Leonid V. Zhigilei [1]

[1)] Department of Materials Science and Engineering, University of Virginia, 395 McCormick Road, Charlottesville, Virginia 22904-4745, USA

[2)] Department of Physics and Astronomy, Aarhus University, Ny Munkegade 120, DK-8000 Aarhus C, Denmark

Abstract

Structural transformations in a shallow surface region of a bulk Ag (001) target irradiated by a femtosecond laser pulse are investigated in large-scale atomistic simulations and experiments. The simulations reveal a complex interplay of fast laser melting, rapid resolidification, and the dynamic relaxation of laser-induced stresses that leads to the formation of a sub-surface porous region covered by a nanocrystalline surface layer. The generation of the porous region is consistent with the experimental observation of surface "swelling" occurring at laser fluences below the spallation/ablation threshold and may be related to the incubation effect in multi-pulse laser ablation of metals. The nanocrystalline layer is produced by massive nucleation of crystallites triggered by a deep undercooling of the melted surface region experiencing fast quenching at a rate on the order of 10^{11} K/s. The predicted surface structure features random crystallographic orientation of nanograins and a high density of stacking faults, twins, and nanoscale twinned structural elements with five-fold symmetry, which suggests high hardness and possible enhancement of catalytic activity of the surface.

Keywords: laser-materials interactions, laser-induced swelling, nanocrystalline materials, twins, incubation effect in laser ablation, pentagonal structural elements, molecular dynamics simulations

I. INTRODUCTION

The ability of short (pico- and femtosecond) pulse laser irradiation to produce unique surface morphologies [1-5], metastable phases [6-8] and microstructure (arrangement of crystal defects) [5,9-14] has been demonstrated in numerous studies and is generally attributed to the conditions of strong electronic, thermal, phase, and mechanical non-equilibrium created in irradiated targets by the fast laser excitation. Detailed understanding of the relations between the basic mechanisms of laser interaction with materials, non-equilibrium processes caused by the fast deposition of laser energy, and the resulting microstructure and properties of laser-treated regions of the targets, however, is still lacking, thus limiting the expansion of laser technologies into the new domain of nanoscale material processing and fabrication. Besides the practical importance, at the fundamental level, the investigations of material response to short-pulse laser irradiation provide unique insights into the peculiarities of material behavior far from equilibrium, under extreme conditions of ultrahigh heating, cooling, and deformation rates.

The small size of the laser-modified zone and the ultrafast rates of processes induced by short pulse laser irradiation present a challenge for experimental probing [15-18] and, at the same time, make atomistic modeling a suitable tool for revealing the mechanisms and pathways of laser-induced structural and phase transformations. The atomistic molecular dynamics (MD) simulation technique has indeed been instrumental in providing valuable information on the microscopic mechanisms of laser melting [19-22], photomechanical spallation and ablation [19,23-29]. Beyond the analysis of the initial dynamic material response to the fast laser energy deposition, however, there has been little progress in extending the simulations to the investigation of processes responsible for the formation of complex surface morphologies and microstructures of the laser-processed targets.

In this paper, we combine large-scale atomistic simulations with experimental characterization of structural changes produced in a single-crystal Ag (001) target by a 100 fs laser pulse irradiation. Based on the simulation results, a pronounced swelling of the irradiated surface observed in experiments is explained by photomechanically-driven generation of sub-surface voids in the transiently melted surface region of the target followed by trapping of the voids by the rapidly advancing solidification front. The ultrafast cooling of the surface region is also found to create the conditions for massive homogeneous nucleation of crystallites and the

formation of a nanocrystalline surface layer with a high density of unusual defect configurations not present in conventional coarse-grained materials. The mechanistic insights into the processes responsible for the unique ability of short laser pulses to produce nanoscale structural changes localized in a thin surface layer of an irradiated target may facilitate the design of new approaches for tailoring surface properties and functionality to the needs of practical applications.

II. COMPUTATIONAL MODEL

TTM-MD model: The large-scale atomistic simulations of laser interactions with a bulk Ag (001) target is performed with a hybrid atomistic–continuum model that couples the classical atomistic molecular dynamics (MD) method with the continuum-level two-temperature model (TTM) [30]. In the original TTM, the time evolution of the lattice and electron temperatures in the irradiated target is described by two coupled nonlinear differential equations that account for the laser excitation of conduction-band electrons, energy exchange between the electrons and atomic vibrations due to the electron-phonon coupling, and the electron heat conduction. In the combined TTM-MD method [19,29], the MD substitutes the TTM equation for the lattice temperature in the surface region of the target, where laser-induced structural and phase transformations take place. The diffusion equation for the electron temperature is solved by a finite difference method simultaneously with MD integration of the equations of motion of atoms. The cells in the finite difference discretization are related to the corresponding volumes of the MD system, and the local lattice temperature is defined for each cell from the average kinetic energy of thermal motion of atoms. The electron temperature enters a coupling term added to the MD equations of motion to account for the energy exchange between the electrons and the lattice [19]. A complete description of the TTM-MD model is provided elsewhere [19,29], and below we only outline the computational setup used in the simulations reported in this paper.

Parameters of the computational system: The atomistic part of the TTM-MD model represents the top 150 nm surface region of the target and consists of 84.2 million Ag atoms arranged into a face-centered cubic (fcc) crystal. In the lateral directions, parallel to the (001) surface of the Ag target, the uniform laser energy deposition and periodic boundary conditions are applied, which mimics the conditions in a small region within a laser spot that is much larger as compared to the lateral dimensions of the computational system, 98.7 nm × 98.7 nm. The lateral

dimensions of the computational system are about twice the dimensions of the largest void observed in the simulation performed in this work at a laser fluence close to the threshold for the void nucleation. The dimensions, therefore, are sufficiently large in this case to avoid an artificial "easy spallation" of the target due to the individual voids outgrowing the size of the computational system. A dynamic pressure-transmitting boundary condition [31,32] is applied at the bottom of the MD system to represent the non-reflecting propagation of the laser-induced stress wave from the MD part of the model into the bulk of the target. Before applying laser irradiation, the Ag crystal is equilibrated at 300 K and the dimensions of the MD computational domain are adjusted to ensure that the initial target is free of internal stresses.

Solution of the TTM equations: The TTM equation for the electron temperature in the atomistic part of the system is solved on a three-dimensional (3D) computational grid with a cell size of 3 nm × 3 nm × 1 nm. The smaller dimension of 1 nm is used in the direction normal to the surface in order to provide an adequate treatment of the strong electron temperature gradient generated by the laser excitation. In the continuum part of the model, beyond the surface region represented by the MD method, the conventional TTM equations for the electron and lattice temperatures are solved on a 3D computational grid with twice larger spacing in the direction normal to the surface. The continuum region is extended down to a depth of 4 μm, so that no significant changes in the electron and lattice temperatures are observed at the bottom of the computational domain during the time of the simulations.

Interatomic potential: The interatomic interactions in the MD part of the model are described by the embedded atom method (EAM) potential with the functional form and parameterization developed in Ref [33]. A cut-off function suggested in Ref. [34] is added to the potential to smoothly bring the interaction energies and forces to zero at interatomic distance of 5.5 Å. Although the potential is fitted to low-temperature values of the equilibrium lattice constant, sublimation energy, elastic constants, and vacancy formation energy, it also provides a good description of high-temperature thermodynamic properties of Ag [35] relevant to the simulation of laser-induced processes. In particular, the equilibrium melting temperature, T_m, determined in liquid–crystal coexistence simulations, is 1139 ± 2 K [8], about 8% below the experimental values of 1235 K [36]. The threshold temperature for the onset of the explosive phase separation into liquid and vapor, T^*, determined in simulations of slow heating of a

metastable liquid, is found to be ~3450 K at zero pressure and ~4850 K at 0.5 GPa [37]. The onset of the phase explosion can be expected at 10% below the critical temperature [38-40] and the values of T^* calculated for the EAM Ag material are not in conflict with the range of experimental values of the critical temperature of Ag spanning from 4300 K to 7500 K [41].

Parameters of the TTM equation for the electron temperature: The electron temperature dependences of the electron-phonon coupling factor and electron heat capacity are taken in the forms that account for the thermal excitation from the electron states below the Fermi level [42]. The electron thermal conductivity is described by the Drude model relationship, $K_e(T_e,T_l) = v^2 C_e(T_e)\tau_e(T_e,T_l)/3$, where $C_e(T_e)$ is the electron heat capacity, v^2 is the mean square velocity of the electrons contributing to the electron heat conductivity, approximated in this work as the Fermi velocity squared, v_F^2, and $\tau_e(T_e,T_l)$ is the total electron scattering time defined by the electron-electron and electron-phonon scattering rates, $1/\tau_e = 1/\tau_{e-e} + 1/\tau_{e-ph} = AT_e^2 + BT_l$. The value of the coefficient A, 3.57×10^6 $s^{-1}K^{-2}$, is estimated within the free electron model, following the approach suggested in [43]. The value of the coefficient B, 1.12×10^{11} $s^{-1}K^{-1}$ is obtained from the experimental value of the thermal conductivity of solid Ag at the melting temperature, 363 $Wm^{-1}K^{-1}$ [44].

Laser excitation: The irradiation of the target with a 100 fs laser pulse is represented through a source term added to the equation for the electron temperature [19]. The source term simulates excitation of the conduction band electrons by a laser pulse with a Gaussian temporal profile and reproduces the exponential attenuation of laser intensity with depth under the surface (Beer–Lambert law). In order to account for the energy transport occurring before the thermalization of the excited electrons [8,45,46], the optical absorption depth, L_p = 12 nm at laser wavelength of 800 nm [47], is combined with the effective depth of the "ballistic" energy transport, L_b = 56 nm, roughly estimated here as a product of the Fermi velocity and the Drude relaxation time [48]. This estimate is in a good agreement with a prediction of 53±7 nm derived from experiment [49]. The effective range of the laser energy deposition is then defined as L_p + L_b = 68 nm and is used in the source term instead of L_p alone. The reflectivity of the surface is not defined in the model since the absorbed laser fluence rather then the incident fluence is used in the discussion of the simulation results.

Structural analysis of atomic configurations: Two methods of structural analysis of atomic configuration are used in this work. The first method is based on the calculation of the local order parameter [19,50] for each atom in the system. The advantage of the local order parameter is that it is computationally inexpensive and can be used for quick on-the-fly analysis of melting and subsequent epitaxial resolidification of a single crystal target during the simulation. The analysis based on the local order parameter fails, however, to identify the nucleation and growth of new crystallites that have crystallographic orientation that is different from the original substrate. This is not surprising since the local order parameter is a measure of the degree of correlation of an atomic configuration to the original crystal structure used as the reference state. The structure of the final surface layer generated by the short pulse laser processing, therefore, is probed with a more complex structural analysis method suggested in Ref. [51] and modified in Ref. [8] to improve the accuracy of identification of crystal structures in the presence of small lattice distortions. This method allows for unambiguous identification of different crystal structures (fcc, bcc, hcp) regardless of their crystallographic orientation.

III. TTM-MD SIMULATION: GENERATION OF SUB-SURFACE VOIDS AND NANOCRYSTALLINE LAYER

The large-scale TTM-MD simulation discussed in this section is performed at an absorbed laser fluence of 0.085 J/cm^2. This fluence is chosen so that the laser pulse produces a substantial modification of the irradiated surface yet does not cause a massive material ejection (spallation or ablation [29]) from the target. The laser-induced processes responsible for the structural modification of the target are illustrated in Fig. 1. The electronic excitation by the 100 fs laser pulse is followed by a rapid energy transfer from the excited electrons to the atomic vibrations. The sharp increase of the strength of the electron-phonon coupling in Ag in the electronically excited state [42] increases the rate of the lattice heating and contributes to the initial confinement of the deposited laser energy in a relatively shallow region of the target. By the time of 10 ps, the material in the top 40 nm surface region of the target is superheated in excess of 20% above the equilibrium melting temperature predicted by the Embedded Atom Method (EAM) description of Ag, T_m = 1139 K [8], and undergoes a rapid homogeneous melting that proceeds in the form of a collapse of the crystal lattice on the timescale of just several picoseconds [19,20]. The short time of the homogeneous melting under the conditions of strong

superheating is consistent with the results of earlier simulations [19-22] and time-resolved electron diffraction experiments [15,52] reported for thin metal films irradiated by femtosecond laser pulses. The fast homogeneous melting results in the formation of a melting front that moves deeper into the target and reaches the maximum depth of 67 nm under the initial surface by the time of ~70 ps.

Meanwhile, the lattice heating due to the equilibration with the excited electrons is succeeded by a rapid cooling due to the high electron thermal conductivity of Ag and sharp temperature gradient generated in the surface region of the target. The temperature at the solid–liquid interface drops below the equilibrium melting temperature of Ag by the time of ~75 ps and the melting turns into resolidification (epitaxial regrowth) of the Ag substrate, as can be seen from the shape of the black curve in Fig. 1a,b that shows the position of the liquid–crystal interface. The release of the latent heat of melting in the solidification process partially offsets the cooling due to the electron heat conduction and results in the locally elevated lattice temperature near the solidification front, Fig. 1a. Note that the finite time of the electron-phonon equilibration causes a few hundred degrees split of the electron and lattice temperatures at the rapidly advancing liquid–crystal interface, an effect that has been observed in earlier simulations of both melting [53] and solidification [12,17] occurring under conditions of strong superheating/undercooling.

The velocity of the resolidification front increases up to the maximum value of about 90 m/s as the temperature at the front drops down to about $0.9T_m$ and then decreases by about a factor of two as the front propagates further up, towards the surface. The value of the maximum velocity of solidification front observed in the simulation is in good agreement with the values estimated from optical pump-probe measurements performed for Ag films [17] and predicted in MD simulations [17,54]. The substantial decrease of the solidification velocity, however, is in conflict with predictions of the MD simulations [17,54], where the velocity of the (001) interface in Ag is predicted to stay at an almost constant (maximum) level at temperatures below $0.85T_m$. The decrease of the velocity of the solidification front, therefore, cannot be attributed to changes in the degree of undercooling at the front and must be related to the dynamic processes occurring in the melted part of the target. These processes, manifesting themselves in the appearance of a low-density region at a depth of ~40 nm under the surface (Fig. 1b), are discussed next.

The fast lattice heating during the first picoseconds after the laser pulse takes place under conditions of stress confinement [23,28,29,55,56], *i.e.*, the heating time is shorter than the time needed for the mechanical equilibration (expansion) of the heated region. As a result, the initial heating takes place under almost isochoric conditions, causing a buildup of high compressive stresses in the surface region of the irradiated target. The sharp rise of the compressive stresses can be seen in Fig. 1c, where the evolution of pressure averaged over a region located between 10 nm and 40 nm from the initial surface is shown. The relaxation of the compressive stresses in the presence of the free surface of the target results in the generation of an unloading wave with tensile stresses increasing with depth under the surface. The tensile stresses, highlighted in Fig 1c by light blue color, are sufficiently strong to induce cavitation in the melted sub-surface region where the combination of the rapid expansion and the temperature increase creates the conditions for the onset of massive nucleation of multiple voids [23,29,55]. The onset of the cavitation limits the maximum level of the tensile stresses that can be supported by the melted material and prolongs the time the tensile stresses are sustained in the region of void formation, Fig. 1c.

The expansion, contraction, and stabilization of the size of the low-density region in the density contour plot, Fig. 1b, are reflecting a complex evolution of the laser-induced voids. To provide more insights into processes occurring in the cavitation region, the individual voids are identified by superimposing atomic configurations generated in the simulation with a 3D grid of cubic cells with a size of 4.5 Å, finding the cells that do not contain any atoms, and defining the voids as clusters of empty cells connected with each other by sharing a common side. With this definition, the smallest void corresponds to a cluster of two neighboring empty cells and has a volume of $2\times(0.45\text{ nm})^3 \approx 0.2\text{ nm}^3$. The result of the application of this procedure is shown in Figs. 1c,d, where the total number of voids N_v and the combined volume of all voids Ω_v are plotted as functions of time. The top-view projections of all voids in the computational system are also shown as insets in Fig. 1d for four moments of time during the simulation.

The plots and the projections can be used to distinguish four stages of the void evolution, as marked at the top of Fig. 1d. First, the rapid rise in the number of small voids is observed between 25 and 55 ps, *i.e.*, during the time when the maximum tensile stresses are generated in the surface region of the target, Fig. 1c. Second, during the time between 55 and 800 ps the

number of voids decreases while the total volume of voids steadily increases. This stage is characterised by the growth and coalescence of large voids and a steadily decreasing population of smaller voids [29,55]. At the same time, the top surface layer of the target, accelerated during the short time of the initial relaxation of the laser-induced compressive stresses (Fig. 1c), gradually slows down its outward motion due to the resistance of the cavitation region to the fast uniaxial expansion. This resistance is reflected in a persistent negative pressure [57], shown in Fig. 1c up to 200 ps, that remains at a level of -25 – -70 MPa up to 800 ps. Only six large voids can be identified at the end of this stage of the void evolution, 800 ps, when the total volume of voids (Fig. 1d), the size of the low-density region affected by the void evolution (Fig. 1b), and the vertical displacement of the surface (Fig. 1a,b) all reach their maximum values.

The third stage of the void evolution is signified by void contraction driven by minimization of the surface energy of the voids. While the number of voids remains the same at this stage, the total volume of the voids decreases by ~23% during the time between 800 and 1400 ps, Fig. 1d. As discussed above, the evolution of voids proceeds simultaneously with rapid advancement of a resolidification front that reaches the bottom of the cavitation region by the time of 500 ps, when the cavitation region is still expanding and the voids are growing. The detailed picture of the resolidification process is provided by snapshots of atomic configurations shown in Fig. 2, where the atoms are colored by their potential energy. By the time of 800 ps, when the voids start to shrink, the bottom part of the cavitation region is already solidified, and the contraction of the voids is affecting the continuously diminishing top part of the cavitation region. The resolidification front reaches the top boundary of the cavitation region by the time of ~1400 ps, signifying transition to the fourth stage of the void evolution, when the voids are fully embedded into the crystalline material and remain stable upon further cooling of the target.

The voids impede the solidification front propagation, as the solidification of the cavitation region involves a relatively slow lateral crystal growth behind the voids. This effect is apparent in a snapshot shown for 1200 ps in Fig. 2, where several regions adjacent to voids are left behind in the melted state while the solidification front advances between the voids. The slowdown of the epitaxial solidification front extends the time the top surface layer of the target remains in the melted state, which results in an increasingly deep undercooling of the melted surface region. At about 1300 ps, when the surface temperature drops down to ~0.69T_m, a massive nucleation of small crystallites is observed throughout the deeply undercooled liquid

region. The fast growth and coalescence of the crystallites leads the formation of a roughly 30 nm thick nanocrystalline surface layer within the following 400 ps, as seen in the snapshots shown in Figs. 2 and 3. The release of the latent heat of melting in the course of the rapid nucleation and growth of the crystallites is also reflected in the transient temperature increase in the surface region of the target outlined by the dashed rectangle in the temperature contour plot shown in Fig. 1a. Note that the position of the liquid–crystal interface shown by black lines in Fig. 1a,b is determined with a method of structural analysis based on the calculation of local order parameter. As discussed in Section II, this method only tracks the advancement of the epitaxial regrowth of the original single crystal target and is "blind" to the appearance of a nanocrystalline surface layer.

IV. EXPERIMENTAL OBSERVATION OF SURFACE SWELLING

The computational prediction of the generation of sub-surface voids frozen in the rapid solidification process, are consistent with our experimental study of the same system: a single-crystal Ag (001) target irradiated by a 100 fs laser pulse. The experiments are undertaken in an ultrahigh vacuum (UHV, ~10^{-9} Torr) chamber. Prior to the laser irradiation, the Ag (001) surfaces are cleaned by a sputter gun with 1 keV Ar^+ ions (~3×10^{-5} Torr) for about an hour, and subsequently annealed at ~940 K for another hour to eliminate possible defects introduced during the sputtering process. To ensure a smooth surface, the sputtering/annealing cycles are repeated 3-5 times. To facilitate comparison with the simulation results, the absorbed rather than incident laser fluence is used in the discussion of the experimental data. The incident fluence is translated to the absorbed one by assuming a reflectivity of 0.969 at the laser wavelength of 800 nm used in the experiments [59]. The laser beam has an elliptical Gaussian spatial profile and the fluence referred here is the peak fluence at the center of the laser spot. The laser spot size is determined in situ by using an approach originally proposed in Ref. [60]. The dimensions of the laser-damaged spots are obtained from a series of scanning electron microscope (SEM) images taken for different laser pulse energies. Since the damage spots are slightly elliptical, the major and minor axes are determined independently from the data fitted to two beam waists and a common threshold energy using an approach described in Ref. [61]. The data provide minor and major spot sizes (*i.e.*, radii at $1/e$ intensity) of 20 ± 2 and 29 ± 2 μm, while the damage threshold fluence is 2.5 ± 0.2 J/cm^2 corresponding to an absorbed fluence of 0.078 ± 0.006 J/cm^2.

Following the sample preparation, the Ag (001) surface is exposed to a single laser pulse, and the irradiated spots are imaged with atomic force microscopy (AFM). An example AFM scan of a spot irradiated at an absorbed laser fluence of 0.15 J/cm^2 and several line scans of spots irradiated at absorbed fluences ranging from 0.098 J/cm^2 to 0.893 J/cm^2 are shown in Fig. 4. A characteristic feature of the scans taken at laser fluences close to the ablation threshold is the formation of pronounced bumps extending above the level of the original surface. The height of the bumps ranges from several hundreds to more than a thousand of nanometers.

The appearance of the bumps can be related to the computational prediction of the generation of sub-surface voids that produce an effective volume increase, or "swelling," of the target. The magnitude of the swelling observed in the simulation, ~17 nm at an absorbed fluence of 0.085 J/cm^2, is much smaller than the ones measured in experiments. This discrepancy can be explained by the difference in the conditions of the material ejection in the simulation and experiments. In the simulations, a small increase of laser fluence from 0.085 J/cm^2 to 0.090 J/cm^2 results in the transition from swelling to the spallation regime, where a 55 nm thick liquid layer is separated from the rest of the target and ejected with a velocity of about 100 m/s. The spallation in this case is facilitated by the use of periodic boundary conditions that allow for the percolation of the growing voids in the lateral direction. In the experiment, the top liquid layer can retain its integrity over large area(s) within the laser spot and the outward motion of the layer in central part of the spot can be restrained by its connection to the colder periphery of the spot, where the conditions for spallation are not achieved. Consequently, the range of laser fluences for which the effect of swelling is observed and the swelling magnitude can both be substantially higher due to the finite laser spot effects. Given the difference in the "boundary conditions" in the simulations and experiments, the computational prediction of the 17-nm swelling at 0.085 J/cm^2 and the spallation onset at 0.090 J/cm^2 is consistent with the experimental observation of the surface swelling by several hundred nanometers at the peak fluence of 0.098 J/cm^2 at the center of the laser spot.

At higher laser fluences, the sub-surface voids in the central part of the spot can be expected to grow, coalesce, and lead to the formation of an increasingly coarse foamy structure underneath the expanding top liquid layer. The subsequent solidification of the transiently melted surface region proceeding simultaneously with the partial recession of the foamy structure is likely to be responsible for the formation of corrugated bumps observed in Fig. 4.

Indeed, given the computational prediction of a shallow (less than 100 nm, see Figs. 1 and 2 for Ag and Ref. [29] for Al) depth of the initial target affected by the void nucleation in the spallation regime and the micron-scale height of the bump, the assumption of the foamy structure of the bump with a density as low as 10% of the one of the solid target appears to be a reasonable conjecture. Due to the coarse-grained nature of the structural features of the surface morphology and the collective nature of processes involved in the generation of the foamy sub-surface structure, the atomistic simulations cannot capture the large-scale swelling at higher fluences, even if a "mosaic approach" [29] combining the results of simulations performed for different local fluences within the laser spot is applied.

All bump profiles shown in Fig. 4b exhibit a characteristic shape of a "volcano" with an increasingly large depression ("crater") in the central part of the spot. While the formation of craters at higher fluences can be associated with the onset of collective material ejection due to spallation or explosive boiling (the simulations predict a transition from spallation to phase explosion at about 2.0 J/cm^2), at lower fluences it may also reflect a partial collapse of the voids. Indeed, the magnitude of swelling in the simulation is defined by the competition between the contraction of the voids (stage 3 of the void evolution discussed above) and their capture by the resolidification front. The central part of the spot receives the highest local fluence and is the last one to solidify, giving more time for the void contraction.

The effect of swelling is not unique to Ag and has also been observed for femtosecond laser irradiation of Al targets [3,62,63], where the presence of sub-surface voids was directly confirmed in transmission electron microscopy (TEM) and scanning electron microscopy (SEM) imaging of cross-sections of the swollen areas of the target [3,63]. The smaller thermal conductivity and larger melting depth at fluences close to the spallation threshold in Al, as compared to Ag, reduce the extent of swelling to about a hundred of nanometers and lead to a partial collapse of the voids prior to solidification, as reflected in the flattening of the void shapes parallel to the surface of the target observed in the TEM and SEM images.

V. SPALLATION BY 2ND PULSE: CONNECTION TO INCUBATION EFFECT

The generation of sub-surface voids is likely to alter the target response to irradiation by subsequent laser pulses and may reduce the threshold fluence for the collective material ejection [3]. To verify this hypothesis, an additional simulation of the 2nd pulse laser irradiation is

performed for the resolidified target obtained by the end of the simulation discussed above. Since a complete cooling of the target down to the ambient temperature can be expected for laser repetition rates of less than MHz, the atomic configuration obtained by the end of the first simulation (at 2 ns after the 1st pulse) is cooled to 300 K with the cooling rate of 2 K/ps before applying the second pulse. All the parameters of the second simulation are identical to the ones used in the first simulation, except for the range of the ballistic energy transport that is reduced from 56 nm in the first simulation (see Section II) to 18 nm. We assume that the presence of the voids and enhancement of the electron scattering by the high density of grain boundaries and crystal defects [64,65] reduces the effective range of the laser energy deposition (the optical absorption depth combined with the ballistic range) down to 30 nm, *i.e.*, the thickness of the nanocrystalline surface layer.

The results of the simulation are illustrated in Figs. 5-8, where the evolution of the thermodynamic parameters is shown along with several snapshots of atomic configurations. The presence of a porous region of sub-surface voids is significantly affecting the laser-induced processes in the surface region of the irradiated target. First, the reduced conductivity of the porous sub-surface region results in the confinement of the deposited laser energy in the top layer of the target, Fig. 5a. The fast heating leads to the generation of high compressive pressure right above the porous region, Fig. 5b. The compressive pressure drives the rapid collapse of the voids during the first 30 ps after the laser pulse, as can be seen from the disappearance of the low-density region initially located between 40 and 70 nm under the surface in the density contour plot, Fig. 5c, as well as from the snapshots shown for 10, 20, and 30 ps in Fig. 6. The void collapse can involve generation of liquid jets and local hot spots in the material, as illustrated in an enlarged view of one of the voids provided in Fig. 7. Indeed, in this case the liquid jet ejected from the top part of the void is accelerated up to a velocity of ~2000 m/s by the time it collides with the solid bottom side of the void, leading to the heating and melting of the underlying crystal. The process of the void collapse is associated with the emission of unloading waves, followed by compression generated at the end of the collapse. The unloading wave propagating toward the surface acts in accord with the unloading wave propagating from the surface of the target and contributes to the rapid expansion of the surface region. The expansion leads to the fast cooling (Fig. 5a), disintegration and ejection of the top region of the target, Figs. 6 and 8.

The maximum temperature in the simulation is about 21% below the threshold temperature for the onset of the phase explosion, 3450 K at zero pressure (see Section II). The material disintegration and ejection, therefore, is driven by the relaxation of the laser induced stresses and has the characteristic features of the conventional spallation process, such as the ejection of a thin liquid followed by small liquid droplets and the absence of any significant amount of the vapor phase in the ablation plume [28,29,55]. A notable observation from this simulation, however, is that the presence of sub-surface voids generated by the first laser pulse brings the absorbed fluence required for the material ejection below the single-pulse spallation threshold. This observation may be related to the incubation effect reported for multi-pulse irradiation of metal targets, when the laser fluence threshold for ablation/damage decreases with increasing number of laser pulses applied to the same area, *e.g.*, [61,65-69]. While the generation and accumulation of defects has been discussed in general terms as one of the mechanisms [12,65-67,70] (along with the absorption enhancement due to roughening of the surface [61,68] and heat accumulation in high repetition rate irradiation [70]) responsible for the incubation effect, the current simulation results provide first direct insights into the laser-induced structural-modification processes that will also contribute to the reduction of the spallation threshold in the multi-pulse laser irradiation regime.

VI. STRUCTURE OF THE NANOCRYSTALLINE SURFACE LAYER

Turning to the analysis of the surface microstructure generated by rapid solidification under highly non-equilibrium conditions of deep undercooling in the simulation of the first pulse irradiation, a clear visual picture of nanocrystalline surface structure is provided in Fig. 9a, where individual nanograins are colored by their crystallographic orientation. Most nanograins have sizes on the order of several nanometers, with several grains extending to tens of nanometers, as shown in the grain size distribution in Fig 9b, where the grain sizes are defined as diameters of spheres with equivalent volumes. The crystallographic orientation of the nanograins appears to be random and unaffected by the presence of the (001) substrate, with no noticeable texture present in the <111> pole figure obtained by collecting stereographic projections of four <111> directions of all fcc atoms in the nano-crystalline layer, Fig. 9b.

To provide further insights into the structure of the nanograins, a method that enables identification of the local structure in the vicinity of each atom in the system (see Section II) is

applied to the final atomic configuration obtained in the simulation of the single-pulse laser irradiation of the target. In Figs. 9c-f the atoms are colored according to their local structural environment, with fcc and hcp atoms colored light blue and green, respectively. A striking observation from Figs. 9c-f is a prominent presence of nanograins with coexisting fcc and hcp regions. The fcc and hcp regions have $<111>_{fcc}//<0001>_{hcp}$ orientation relationship and form a characteristic striped close-packed structure composed of alternating fcc and hcp platelets extending throughout the nanograins, *e.g.*, a nanograin shown in the lower right part of Fig. 9f. These nanograins can also be considered as having fcc structure with a high density of aligned stacking faults, with stacking faults present on every other plane within the hcp regions. Some of the nanograins exhibit an apparently random mixture of fcc- and hcp-like stacking of close-packed planes that has been observed experimentally in hard-sphere colloidal crystals [70-72] and atomistic simulations [73-75]. The coexistence of fcc and hcp grains has been observed in pulsed laser deposited nanocrystalline Ni films [77], where the formation of stacking faults on in-plain {111} fcc faces in the process of film deposition is considered to be the mechanism leading to the formation of hcp grains. A similar process of cross-nucleation of the hcp phase on {111} faces of an fcc nucleus growing in an undercooled liquid has been predicted in atomistic simulations [74]. The highly non-equilibrium nature of the rapid solidification process, along with the low stacking-fault energy of Ag [78] are the factors facilitating the generation of a high density of the stacking faults and the mixed fcc-hcp structures.

Another type of structural elements revealed by the analysis of the atomic structure are polydecahedral structures exhibiting multiple axes of non-crystallographic five-fold symmetry, *e.g.*, Figs. 9d-f. Each fivefold axis is formed by a local decahedral arrangement of five fcc domains aligned along a common <110> axis and joined together along {111} planes. The boundaries between the neighboring domains are coherent twin boundaries with local atomic structure of hcp planes. As a result, the pentagonal structural elements show up in Figs. 9d-f as five atomic planes with local hcp structure (colored green) radiating from a common axis. The angle between two close-packed {111} planes in the FCC lattice is 70.53º and packing of perfect fcc domains into the pentagonal structure leaves 360º – 70.53º×5 = 7.35º solid angle deficiency. Closing the gap in the packing of the fcc domains introduces inhomogeneous strain into the system and is equivalent to the introduction of a positive wedge disclination with a power of 7.35º [79,80]. The strong quadratic dependence of the elastic strain energy of a disclination on

the size of the crystal precludes the five-fold twinned structures from appearing in bulk crystals and largely limits their habitat to nanoparticles and nanowires with sizes up to several tens of nanometers [79,80-83]. The pentagonal twinned structures have also been reported for nanocrystalline metals synthesized by severe plastic deformation techniques [84-86], where the formation of the fivefold deformation twins is attributed to a sequential twinning occurring under conditions of changing orientation of external stresses [87,88]. Alternatively, the generation of high internal local stresses during annealing of nanocrystalline Cu has been predicted to lead to the formation of fivefold twins in MD simulations [89]. In contrast to these earlier reports, the pentagonal structural elements observed in the nanocrystalline layer generated in the short-pulse laser processing are not produced through the deformation twinning but are formed in the process of rapid solidification of strongly undercooled liquid. The appearance of these twinned structures can be explained by the favorable kinetic pathways for the nucleation of pentagonal structures revealed in MD simulations of nanoparticles [75,76,90], as well as an effective screening of the elastic energy of the disclinations due to the small size of the nanograins and the presence of other crystal defects.

The computational prediction of the formation of a thin nanocrystalline layer with high density of stacking faults, twins, and pentagonal twinned structures suggests the short pulse laser processing as a viable alternative to the severe plastic deformation [91,92] or pulsed electrodeposition [93] techniques that are currently yielding the maximum structural refinement and high strength of metal samples. Moreover, the localization of the nanocrystalline layer within a thin surface layer of the target and the prominent presence of twin boundaries and pentagonal structural elements are two factors that may also increase the ductility of the laser-modified layer, a property that is generally incompatible with high strength. Indeed, a simultaneous enhancement of strength and ductility has been demonstrated for nanotwinned metals [93-95] as well as for materials with gradient microstructure varying from nanograined surface to coarse-grained interior [97,98]. Beyond the mechanical properties, the high sensitivity of catalytic activity of metal surfaces and nanoparticles to their atomic structure [99,100] suggests that the presence of a broad spectrum of atomic configurations on nanostructured surfaces produced by femtosecond laser processing may lead to an enhanced catalytic activity of the surface. The presence of twins, in particular, have been found to result in a substantial

enhancement of hydrogen absorption [101] and electrocatalitic activity of icosahedral nanoparticles [102,103].

VII. SUMMARY

In summary, a joint computational – experimental study of structural modification of the (001) surface of a single-crystal Ag target irradiated by a femtosecond laser pulse reveals the microscopic mechanisms responsible for the generation of complex surface nano-structure at laser fluences below the spallation threshold. A pronounced swelling of the irradiated surface observed in experiments is explained by results of a large-scale atomistic simulation, where a concurrent occurrence of fast laser melting, generation and dynamic relaxation of laser-induced stresses, and rapid cooling and resolidification of the transiently melted surface region of the target is found to produce a sub-surface porous region covered by a nanocrystalline layer. The presence of sub-surface voids generated by single-pulse laser irradiation reduces the threshold fluence for the spallation onset for subsequent pulses, suggesting the generation of voids as a plausible mechanism responsible for the incubation effect observed in multi-pulse laser ablation of metals. The top nanocrystalline layer, produced by massive nucleation of new crystallites under conditions of deep undercooling, contains a high density of stacking faults, twins, and pentagonal twinned structural elements, suggesting a high hardness and possible enhancement of catalytic activity of the surface. The unique ability of short laser pulses to produce nanoscale structural changes localized in a thin surface layer of an irradiated target is providing new opportunities for tailoring surface properties and functionality to the needs of practical applications.

Acknowledgments: Financial support for this work was provided by the National Science Foundation (NSF) through Grants DMR-0907247 and CMMI-1301298, and the Air Force Office of Scientific Research through Grant FA9550-10-1-0541. Computational support was provided by the Oak Ridge Leadership Computing Facility (Projects MAT048) and NSF through the Extreme Science and Engineering Discovery Environment (Project TG-DMR110090). The experimental work has been supported by Danish Council for Independent Research | Natural Sciences (FNU).

References

1. A. Y. Vorobyev and C. Guo, Enhanced absorptance of gold following multipulse femtosecond laser ablation, *Phys. Rev. B* **72**, 195422 (2005).
2. Q.-Z. Zhao, S. Malzer, and L.-J. Wang, Self-organized tungsten nanospikes grown on subwavelength ripples induced by femtosecond laser pulses, *Opt. Express* **15**, 15741-15746 (2007).
3. J.-M. Savolainen, M. S. Christensen, and P. Balling, Material swelling as the first step in the ablation of metals by ultrashort laser pulses, *Phys. Rev. B* **84**, 193410 (2011).
4. Y. Dai, M. He, H. Bian, B. Lu, X. Yan, and G. Ma, Femtosecond laser nanostructuring of silver film, *Appl. Phys. A* **106**, 567-574 (2012).
5. J. V. Oboňa, V. Ocelík, J. C. Rao, J. Z. P. Skolski, G. R. B. E. Römer, A. J. Huis in 't Veld, and J. Th. M. De Hosson, Modification of Cu surface with picosecond laser pulses, *Appl. Surf. Sci.* **303**, 118-124 (2014).
6. C. J. Lin and F. Spaepen, Nickel-niobium alloys obtained by picosecond pulsed laser quenching, *Acta Metall.* **34**, 1367-1375 (1986).
7. A. Vailionis, E. G. Gamaly, V. Mizeikis, W. Yang, A. V. Rode, and S. Juodkazis, Evidence of superdense aluminium synthesized by ultrafast microexplosion, *Nat. Commun.* **2**, 445 (2011).
8. C. Wu, D. A. Thomas, Z. Lin, and L. V. Zhigilei, Runaway lattice-mismatched interface in an atomistic simulation of femtosecond laser irradiation of Ag film - Cu substrate system, *Appl. Phys. A* **104**, 781-792 (2011).
9. A. Weck, T. H. R. Crawford, A. Borowiec, D. S. Wilkinson, and J. S. Preston, Femtosecond laser-based fabrication of a new model material to study fracture, *Appl. Phys. A* **86**, 55-61 (2007).
10. A. Kumar and T. M. Pollock, Mapping of femtosecond laser-induced collateral damage by electron backscatter diffraction, *J. Appl. Phys.* **110**, 083114 (2011).
11. D. S. Ivanov, B. Rethfeld, G. M. O'Connor, Th. J. Glynn, A. N. Volkov, and L. V. Zhigilei, The mechanism of nanobump formation in femtosecond pulse laser nanostructuring of thin metal films, *Appl. Phys. A* **92**, 791-796 (2008).
12. Z. Lin, R. A. Johnson, and L. V. Zhigilei, Computational study of the generation of crystal defects in a bcc metal target irradiated by short laser pulses, *Phys. Rev. B* 77, 214108 (2008).
13. X. Sedao, C. Maurice, F. Garrelie, J.-P. Colombier, S. Reynaud, R. Quey, G. Blanc, and F. Pigeon, Electron backscatter diffraction characterization of laser-induced periodic surface structures on nickel surface, *Appl. Surf. Sci.* **302**, 114-117 (2014).
14. X. Sedao, C. Maurice, F. Garrelie, J.-P. Colombier, S. Reynaud, R. Quey, and F. Pigeon, Influence of crystal orientation on the formation of femtosecond laser-induced periodic surface structures and lattice defects accumulation, *Appl. Phys. Lett.* **104**, 171605 (2014).

15. B. J. Siwick, J. R. Dwyer, R. E. Jordan, and R. J. D. Miller, An atomic-level view of melting using femtosecond electron diffraction, *Science* **302**, 1382-1385 (2003).

16. R. Ernstorfer, M. Harb, C. T. Hebeisen, G. Sciaini, T. Dartigalongue, and R. J. D. Miller, The formation of warm dense matter: experimental evidence for electronic bond hardening in gold, *Science* **323**, 1033-1037 (2009).

17. W. L. Chan, R. S. Averback, D. G. Cahill, and Y. Ashkenazy, Solidification velocities in deeply undercooled silver, *Phys. Rev. Lett.* **102**, 095701 (2009).

18. J. Chen, W.-K. Chen, J. Tang, and P. M. Rentzepis, Time-resolved structural dynamics of thin metal films heated with femtosecond optical pulses, *Proc. Natl. Acad. Sci. USA* **108**, 18887-18892 (2011).

19. D. S. Ivanov and L. V. Zhigilei, Combined atomistic-continuum modeling of short pulse laser melting and disintegration of metal films, *Phys. Rev. B* **68**, 064114 (2003).

20 D. S. Ivanov and L. V. Zhigilei, Effect of pressure relaxation on the mechanisms of short-pulse laser melting, *Phys. Rev. Lett.* **91**, 105701 (2003).

21. Z. Lin and L. V. Zhigilei, Time-resolved diffraction profiles and atomic dynamics in short-pulse laser-induced structural transformations: Molecular dynamics study, *Phys. Rev. B* **73**, 184113 (2006).

22. Z. Lin, E. Leveugle, E. M. Bringa, and L. V. Zhigilei, Molecular dynamics simulation of laser melting of nanocrystalline Au, *J. Phys. Chem. C* **114**, 5686-5699 (2010).

23. L. V. Zhigilei and B. J. Garrison, Microscopic mechanisms of laser ablation of organic solids in the thermal and stress confinement irradiation regimes, *J. Appl. Phys.* **88**, 1281-1298 (2000).

24. X. Wang and X. Xu, Molecular dynamics simulation of heat transfer and phase change during laser material interaction, *J. Heat Transfer* **124**, 265-274 (2002).

25. P. Lorazo, L. J. Lewis, and M. Meunier, Thermodynamic pathways to melting, ablation, and solidification in absorbing solids under pulsed laser irradiation, *Phys. Rev. B* **73**, 134108 (2006).

26. C. Schäfer, H. M. Urbassek, and L. V. Zhigilei, Metal ablation by picosecond laser pulses: A hybrid simulation, *Phys. Rev. B* **66**, 115404 (2002).

27. B. J. Demaske, V. V. Zhakhovsky, N. A. Inogamov, and I. I. Oleynik, Ablation and spallation of gold films irradiated by ultrashort laser pulses, *Phys. Rev. B* **82**, 064113 (2010).

28. L. V. Zhigilei, Z. Lin, and D. S. Ivanov, Atomistic modeling of short pulse laser ablation of metals: Connections between melting, spallation, and phase explosion, *J. Phys. Chem. C* **113**, 11892-11906 (2009).

29. C. Wu and L. V. Zhigilei, Microscopic mechanisms of laser spallation and ablation of metal targets from large-scale molecular dynamics simulations, *Appl. Phys. A* **114**, 11-32 (2014).

30. S. I. Anisimov, B. L. Kapeliovich, and T. L. Perel'man, Electron emission from metal surfaces exposed to ultrashort laser pulses, *Sov. Phys. JETP* **39**, 375-377 (1974).

31. L. V. Zhigilei and B. J. Garrison, Pressure waves in microscopic simulations of laser ablation, *Mat. Res. Soc. Symp. Proc.* **538**, 491-496 (1999).

32. C. Schafer, H. M. Urbassek, L. V. Zhigilei, and B. J. Garrison, Pressure-transmitting boundary conditions for molecular dynamics simulations, *Comp. Mater. Sci.* **24**, 421-429 (2002).

33. S. M. Foiles, M. I. Baskes, and M. S. Daw, Embedded-atom-method functions for the fcc metals Cu, Ag, Au, Ni, Pd, Pt, and their alloys, *Phys. Rev. B* **33**, 7983-7991 (1986).

34. A. F. Voter and S. P. Chen, Accurate interatomic potentials for Ni, Al, and Ni_3Al, *Mat. Res. Soc. Symp. Proc.* **82**, 175-180 (1999).

35. S. M. Foiles and J. B. Adams, Thermodynamic properties of fcc transition metals as calculated with embedded-atom method, *Phys. Rev. B* **40**, 5909-5915 (1989).

36. R.C. Weast (ed.), *Handbook of Chemistry and Physics*, 64th edn. (CRC Press, Boca Raton, 1983).

37. E. T. Karim, M. Shugaev, C. Wu, Z. Lin, R. F. Hainsey, and L. V. Zhigilei, Atomistic simulation study of short pulse laser interactions with a metal target under conditions of spatial confinement by a transparent overlayer, *J. Appl. Phys.* **115**, 183501 (2014).

38. B. J. Garrison, T. E. Itina, and L. V. Zhigilei, The limit of overheating and the threshold behavior in laser ablation, *Phys. Rev. E* **68**, 041501 (2003).

39. A. Miotello and R. Kelly, Laser-induced phase explosion: new physical problems when a condensed phase approaches the thermodynamic critical temperature, *Appl. Phys. A* **69**, S67-S73 (1999).

40. N. M. Bulgakova and A. V. Bulgakov, Pulsed laser ablation of solids: transition from normal vaporization to phase explosion, *Appl. Phys. A* **73**, 199-208 (2001).

41. R. W. Ohse and H. von Tippelskirch, The critical constants of the elements and of some refractory materials with high critical temperatures. (A review), *High Temp.-High Press.* **9**, 367-385 (1977).

42. Z. Lin, L. V. Zhigilei, and V. Celli, Electron-phonon coupling and electron heat capacity of metals under conditions of strong electron-phonon nonequilibrium, *Phys. Rev. B* **77**, 075133 (2008).

43. R. H. M. Groeneveld, R. Sprik, and A. Lagendijk, Femtosecond spectroscopy of electron-electron and electron-phonon energy relaxation in Ag and Au, *Phys. Rev. B* **51**, 11433-11445 (1995).

44. K. C. Mills, B. J. Monaghan, and B. J. Keene, Thermal conductivities of molten metals: Part 1 Pure metals, *Int. Mater. Rev.* **41**, 209-242 (1996).

45. G. Tas and H. J. Maris, Electron diffusion in metals studied by picosecond ultrasonics, *Phys. Rev. B* **49**, 15049-15054 (1994).

46. J. Hohlfeld, S.-S.Wellershoff, J. Güdde, U. Conrad, V. Jähnke, and E. Matthias, Electron and lattice dynamics following optical excitation of metals, *Chem. Phys.* **251**, 237-258 (2000).

47. D. Bäuerle, Laser Processing and Chemistry (Springer-Verlag, Berlin Heidelberg, 2000).

48. N. W. Ashcroft and N. D. Mermin, *Solid State Physics* (Holt, Rinehart and Winston, New York, 1976).

49. J. Byskov-Nielsen, J.-M. Savolainen, M. S. Christensen, and P. Balling, Ultra-short pulse laser ablation of copper, silver and tungsten: experimental data and two-temperature model simulations, *Appl. Phys. A* **103**, 447-453 (2011).

50. J. R. Morris and X. Song, The melting lines of model systems calculated from coexistence simulations, *J. Chem. Phys.* **116**, 9352-9358 (2002).

51. G. J. Ackland, A. P. Jones, Applications of local crystal structure measures in experiment and simulation, *Phys. Rev. B* **73**, 054104 (2006).

52. J. R. Dwyer, R. E. Jordan, C. T. Hebeisen, M. Harb, R. Ernstorfer, T. Dartigalongue, and R. J. D. Miller, Femtosecond electron diffraction: an atomic perspective of condensed phase dynamics, *J. Mod. Optics* **54**, 905-922 (2007).

53. D. S. Ivanov and L. V. Zhigilei, Kinetic limit of heterogeneous melting in metals, *Phys. Rev. Lett.* **98**, 195701 (2007).

54. Y. Ashkenazy and R. S. Averback, Kinetic stages in the crystallization of deeply undercooled body-centered-cubic and face-centered-cubic metals, *Acta Mater.* **58**, 524–530 (2010).

55. E. Leveugle, D. S. Ivanov, and L. V. Zhigilei, Photomechanical spallation of molecular and metal targets: molecular dynamics study, *Appl. Phys. A* **79**, 1643-1655 (2004).

56. G. Paltauf and P. E. Dyer, Photomechanical processes and effects in ablation, *Chem. Rev.* **103**, 487-518 (2003).

57. D. H. Trevena, *Cavitation and Tension in Liquids* (Adam Hilger: Bristol and Philadelphia, 1987)

58. See Supplemental Material at [URL will be inserted by publisher] for animated sequences of snapshots from the simulations illustrated in Figures 2, 6, 7, and 8.

59. D. Bäuerle, Laser Processing and Chemistry (Springer-Verlag, Berlin Heidelberg, 2000).

60. J. M. Liu, Simple technique for measurements of pulsed Gaussian-beam spot sizes, *Opt. Lett.* **7**, 196-198 (1982).

61. J. Byskov-Nielsen, J.-M. Savolainen, M. S. Christensen, and P. Balling, Ultra-short pulse laser ablation of metals: threshold fluence, incubation coefficient and ablation rates, *Appl. Phys. A* **101**, 97-101 (2010).

62. A. A. Ionin, S. I. Kudryashov, A. E. Ligachev, S. V. Makarov, L. V. Seleznev, and D. V. Sinitsyn, Nanoscale cavitation instability of the surface melt along the grooves of one-dimensional nanorelief gratings on an aluminum surface, *JETP Lett.* **94**, 266-269 (2011).

63. S. I. Ashitkov, N. A. Inogamov, V. V. Zhakhovskii, Yu. N. Emirov, M. B. Agranat, I. I. Oleinik, S. I. Anisimov, and V. E. Fortov, Formation of nanocavities in the surface layer of an aluminum target irradiated by a femtosecond laser pulse, *JETP Lett.* **95**, 176-181 (2012).

64. H. E. Elsayed-Ali, T. Juhasz, G. O. Smith, and W. E. Bron, Femtosecond thermoreflectivity and thermotransmissivity of polycrystalline and single-crystalline gold films, *Phys. Rev. B* **43**, 4488-4491 (1991).

65. J. L. Hostetler, A. N. Smith, D. M. Czajkowsky, and P. M. Norris, Measurement of the electron-phonon coupling factor dependence on film thickness and grain size in Au, Cr, and Al, *Appl. Opt.* **38**, 3614-3620 (1999).

66. Y. Jee, M. F. Becker, and R. M. Walser, Laser-induced damage on single-crystal metal surfaces, *J. Opt. Soc. Am. B* **5**, 648-659 (1988).

67. P. T. Mannion, J. Magee, E. Coyne, G. M. O'Connor, and T. J. Glynn, The effect of damage accumulation behaviour on ablation thresholds and damage morphology in ultrafast laser micro-machining of common metals in air, *Appl. Surf. Sci.* **233**, 275-287 (2004).

68. S. E. Kirkwood, A. C. van Popta, Y. Y. Tsui, and R. Fedosejevs, Single and multiple shot near-infrared femtosecond laser pulse ablation thresholds of copper, *Appl. Phys. A* **81**, 729-735 (2005).

69. J. Krüger, D. Dufft, R. Koter, and A. Hertwig, Femtosecond laser-induced damage of gold films, *Appl. Surf. Sci.* **253**, 7815-7819 (2007).

70. G. Raciukaitis, M. Brikas, P. Gecys, and M. Gedvilas, Accumulation effects in laser ablation of metals with high-repetition rate lasers, *Proc. SPIE* **7005**, 70052L (2008).

71. P. N. Pusey, W. van Megen, P. Bartlett, B. J. Ackerson, J. G. Rarity, and S. M. Underwood, Structure of crystals of hard colloidal spheres, *Phys. Rev. Lett.* **63**, 2753-2756 (1989).

72. J. Zhu, M. Li, R. Rogers, W. Meyer, R. H. Ottewill, STS-73 Space Shuttle Crew, W. B. Russel, and P. M. Chaikin, Crystallization of hard-sphere colloids in microgravity, *Nature* **387**, 883-885 (1997).

73. U. Gasser, E. R. Weeks, A. Schofield, P. N. Pusey, and D. A. Weitz, Real-space imaging of nucleation and growth in colloidal crystallization, *Science* **292**, 258-262 (2001).

74. C. Desgranges and J. Delhommelle, Molecular mechanism for the cross-nucleation between polymorphs, *J. Am. Chem. Soc.* **128**, 10368-10369 (2006).

75. C. C. Asuquo and R. K. Bowles, Molecular dynamics simulations of competitive freezing in gold nanoclusters, *J. Phys. Chem. C* **116**, 14619–14626 (2012).

76. H.-J. Zhang, S.-M. Peng, X.-S. Zhou, and X. Ju, Polymorphic crystals selected in the nucleation stage, *Europhys. Lett.* **107**, 46002 (2014).

77. S. Rajasekhara, K. J. Ganesh, K. Hattar, J. A. Knapp, and P. J. Ferreira, Evidence of metastable hcp phase grains in as-deposited nanocrystalline nickel films, *Scripta Mater.* **67**, 189–192 (2012).

78. C. Deng and F. Sansoz, Fundamental differences in the plasticity of periodically twinned nanowires in Au, Ag, Al, Cu, Pb and Ni, *Acta Mater.* **57**, 6090–6101 (2009).

79. V. G. Gryaznov, J. Heydenreich, A. M. Kaprelov, S. A. Nepijko, A. E. Romanov, and J. Urban, Pentagonal symmetry and disclinations in small particles, *Cryst. Res. Technol.* **34**, 1091-1119 (1999).

80. A. E. Romanov, and A. L. Kolesnikova, Application of disclination concept to solid structures, *Prog. Mater. Sci.* **54**, 740-769 (2009)

81. Y. Gao, L. Song, P. Jiang, L. F. Liu, X. Q. Yan, Z. P. Zhou, D. F. Liu, J. X. Wang, H. J. Yuan, Z. X, Zhang, X. W. Zhao, X. Y, Zhou, W. Y. Zhou, G. Wang, S. S. Xie, H. Y. Chen, and J. Q. Li, Silver nanowires with five-fold symmetric cross-section, *J. Cryst. Growth* **276**, 606-612 (2005).

82. Y. Gao, P. Jiang, L. Song, J. X. Wang, L. F. Liu, D. F. Liu, Y. J. Xiang, Z. X. Zhang, X. W. Zhao, X. Y. Dou, S. D. Luo, W. Y. Zhou, and S. S. Xie, Studies on silver nanodecahedrons synthesized by RVP-assisted N, N-dimethylformamide (DMF) reduction, *J. Cryst. Growth* **289**, 376-380 (2006).

83. C. L. Johnson, E. Snoeck, M. Ezcurdia, B. Rodríguez-González, I. Pastoriza-Santos, L. M. Liz-Marzán and M. J. Hÿtch, Effects of elastic anisotropy on strain distributions in decahedral gold nanoparticles, *Nat. Mater.* **7**, 120-124 (2007).

84. J. Monk, J. J. Hoyt, and D. Farkas, Metastability of multitwinned Ag nanorods: Molecular dynamics study, *Phys. Rev. B* **78**, 024112 (2008).

85. J. Y. Huang, Y. K. Wu, and H. Q. Ye, Deformation structures in ball milled copper, *Acta Mater.* **44**, 1211-1221 (1996).

86. X. H. An, Q. Y. Lin, S. D. Wu, Z. F. Zhang, R. B. Figueiredo, N. Gao, and T. G. Langdon, Formation of fivefold deformation twins in an ultrafine-grained copper alloy processed by high-pressure torsion, *Scripta Mater.* **64**, 249-252 (2011).

87. Y. T. Zhu, X. Z. Liao, and X. L. Wu, Deformation twinning in nanocrystalline materials, *Prog. Mater. Sci.* **57**, 1-62 (2012).

88. Y. T. Zhu, X. Z. Liao, and R. Z. Valiev, Formation mechanism of fivefold deformation twins in nanocrystalline face-centered-cubic metals, *Appl. Phys. Lett.* **86**, 103112 (2005).

89. E. M. Bringa, D. Farkas, A. Caro, Y. M. Wang, J. McNaney, and R. Smith, Fivefold twin formation during annealing of nanocrystalline Cu, *Scripta Mater.* **59**, 1267-1270 (2008).

90. G. Rossi and R. Ferrando, Freezing of gold nanoclusters into poly-decahedral structures, *Nanotechnology* **18**, 225706 (2007).

91. R. Z. Valiev, R. K. Islamgaliev, and I. V. Alexandrov, Bulk nanostructured materials from severe plastic deformation, *Prog. Mater. Sci.* **45**, 103-189 (2000).

92. D. A. Hughes and N. Hansen, Exploring the limit of dislocation based plasticity in nanostructured metals*, Phys. Rev. Lett.* **112**, 135504 (2014).

93. L. Lu, Y. Shen, X. Chen, L. Qian, and K. Lu, Ultrahigh strength and high electrical conductivity in copper, *Science* **304**, 422-426 (2004).

94. M. Dao, L. Lu, Y. Shen, and S. Suresh, Strength, strain-rate sensitivity and ductility of copper with nanoscale twins. *Acta Mater.* **54**, 5421-5432 (2006).

95. L. Lu, X. Chen, X. Huang, and K. Lu, Revealing the maximum strength in nanotwinned copper, *Science* **323**, 607-610 (2009).

96. D. Jang, X. Li, H. Gao, and J. R. Greer, Deformation mechanisms in nanotwinned metal nanopillars, *Nat. Nanotechnol.* **7**, 594-601 (2012).

97. T. H. Fang, W. L. Li, N. R. Tao, and K. Lu, Revealing extraordinary intrinsic tensile plasticity in gradient nano-grained copper, *Science* **331**, 1587-1590 (2011).

98. X. Wu, P. Jiang, L. Chen, F. Yuan, and Y. T. Zhu, Extraordinary strain hardening by gradient structure, *Proc. Natl. Acad. Sci. U. S. A.* **111**, 7197-7201 (2014).

99. J. K. Nørskov, T. Bligaard, B. Hvolbæk, F. Abild-Pedersen, I. Chorkendorff, and C. H. Christensen, The nature of the active site in heterogeneous metal catalysis, *Chem. Soc. Rev*. **37**, 2163-2171 (2008).

100. H. Falsig, B. Hvolbæk, I. S. Kristensen, T. Jiang, T. Bligaard, C. H. Christensen, and J. K. Nørskov, Trends in the catalytic CO oxidation activity of nanoparticles, *Angew. Chem.* **120**, 4913-4917 (2008).

101. F. Calvo and A. Carre, Structural transitions and stabilization of palladium nanoparticles upon hydrogenation, *Nanotechnology* **17**, 1292-1299 (2006).

102. T. Lv, Y. Wang, S. Choi, M. Chi, J. Tao, L. Pan, C. Huang, Y. Zhu, and Y. Xia, Controlled synthesis of nanosized palladium icosahedra and their catalytic activity towards formic-acid oxidation, *ChemSusChem* **6**, 1923-1930 (2013).

103. J. Wu, L. Qi, H. You, A. Gross, J. Li, and H. Yang, Icosahedral platinum alloy nanocrystals with enhanced electrocatalytic activities, *J. Am. Chem. Soc.* **134**, 11880-11883 (2012).

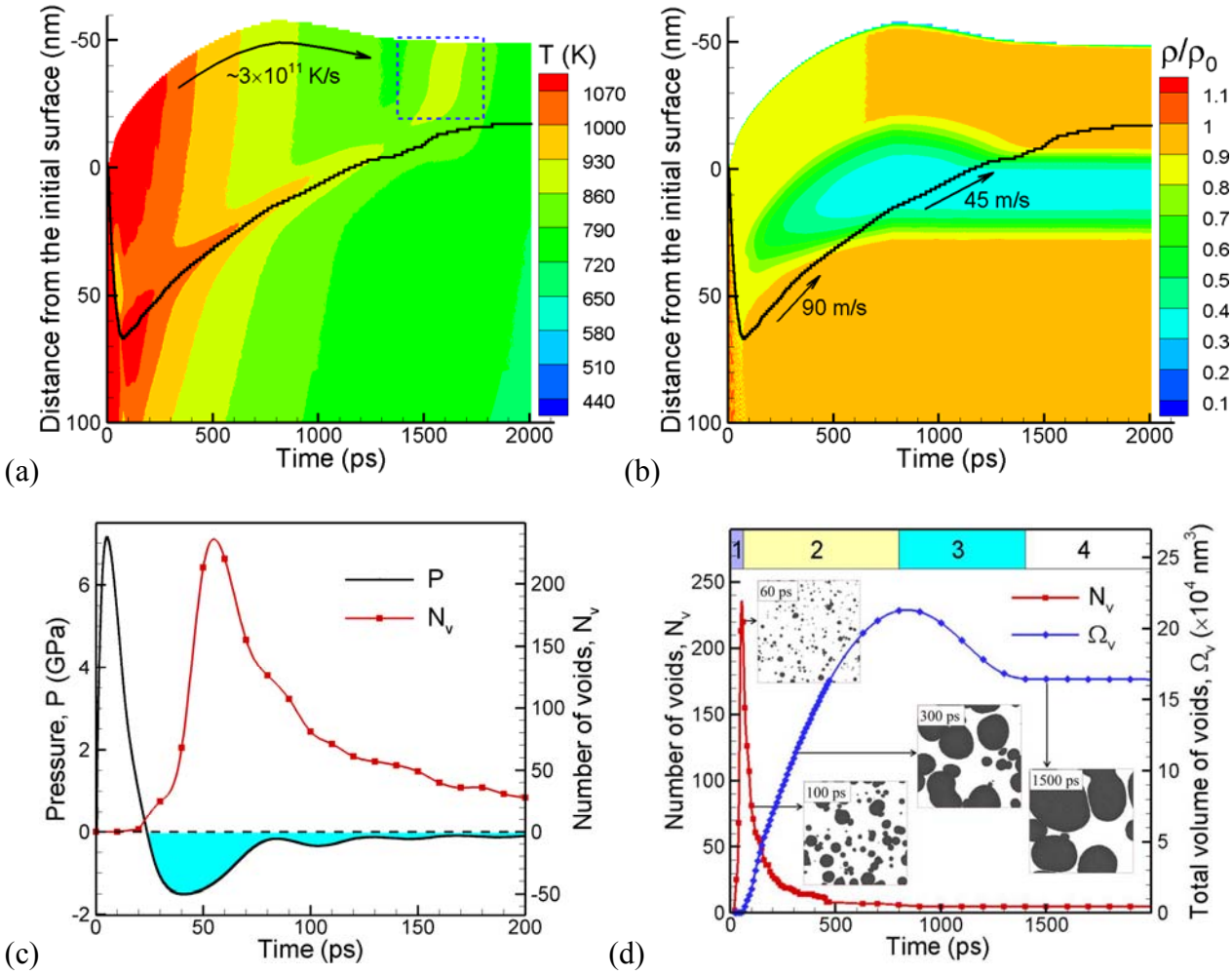

Figure 1: The evolution of thermodynamic parameters and voids in the surface region of a Ag (001) target irradiated by a 100 fs laser pulse at an absorbed fluences of 0.085 J/cm^2. The lattice temperature and density contour plots are shown in (a) and (b) for the top part of the irradiated target, down to the depth of 100 nm below the initial surface. The density in (b) is normalized to the density ρ_0 of Ag at 300 K. The black lines separate the melted (and nanocrystalline) regions from the crystalline bulk of the target. The dashed blue rectangle in (a) marks the time and location of the transient temperature increase due to the rapid nucleation and growth of new crystallites. The cooling rate of the surface region and characteristic velocities of the resolidification front propagation are shown by arrows in (a) and (b), respectively. The evolution of pressure P and total number of voids N_v during the time of the initial target response to the laser irradiation is shown in (c). The pressure is averaged over the region between 10 nm and 40 nm under the initial surface. The negative (tensile) pressure is highlighted by light blue color. The longer-term evolution of the total number of voids N_v and the total volume of voids Ω_v is shown in (d), with the insets showing top-view projections of all voids in the system. Four stages of void evolution can be distinguished, as indicated in (d): stage 1 of void nucleation, stage 2 of void growth/coalescence, stage 3 of void contraction, and stage 4 of stable voids captured by the resolidification front.

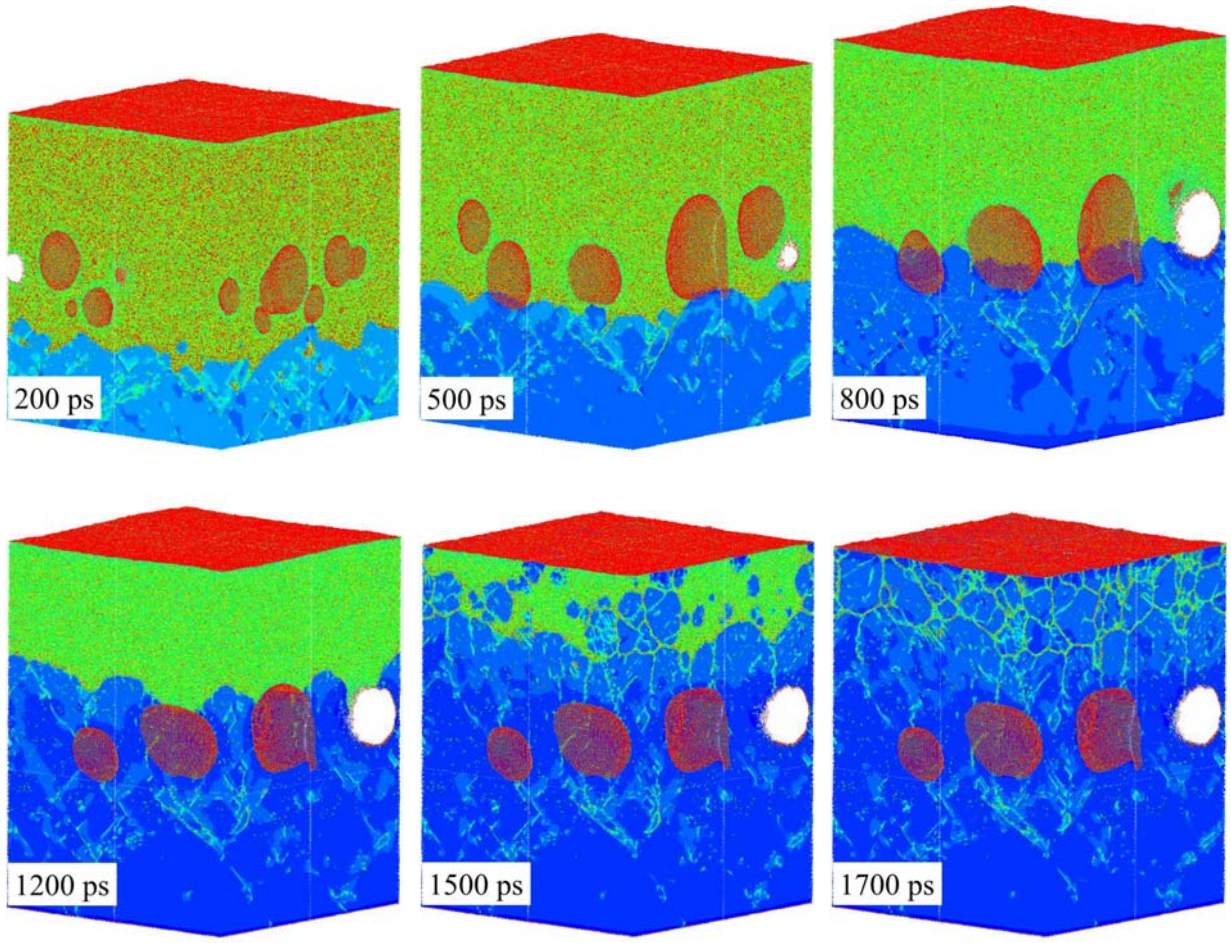

Figure 2: Snapshots of atomic configurations generated in a TTM-MD simulation of Ag (001) target irradiated by a 100 fs laser pulse at an absorbed fluence of 0.085 J/cm^2. Only the top parts of the simulated system, down to a depth of 80 nm below the initial surface are shown in the snapshots. To reduce thermal noise in atomic positions and energies, the atomic configurations are quenched for 0.2 ps using the velocity-dampening technique. The atoms are then colored by their potential energies, with the scale from -2.84 eV (blue) to -2.65 eV (red). This scale ensures that most atoms in the crystalline part of the target are blue, the atoms in the melted part are green, and the atoms on free surfaces are red. The resolidification front crosses the region where the voids are evolving between 500 and 1400 ps. Massive nucleation of small crystallites takes place in the strongly undercooled surface region between 1300 and 1700 ps, leading to the formation of nanocrystalline structure of the top surface layer. The grain boundaries separating nanograins can be identified as regions (lines) of elevated potential energy in the last snapshot. An animated sequence of snapshots from this simulation with a time resolution of 100 ps can be found at Ref. [58].

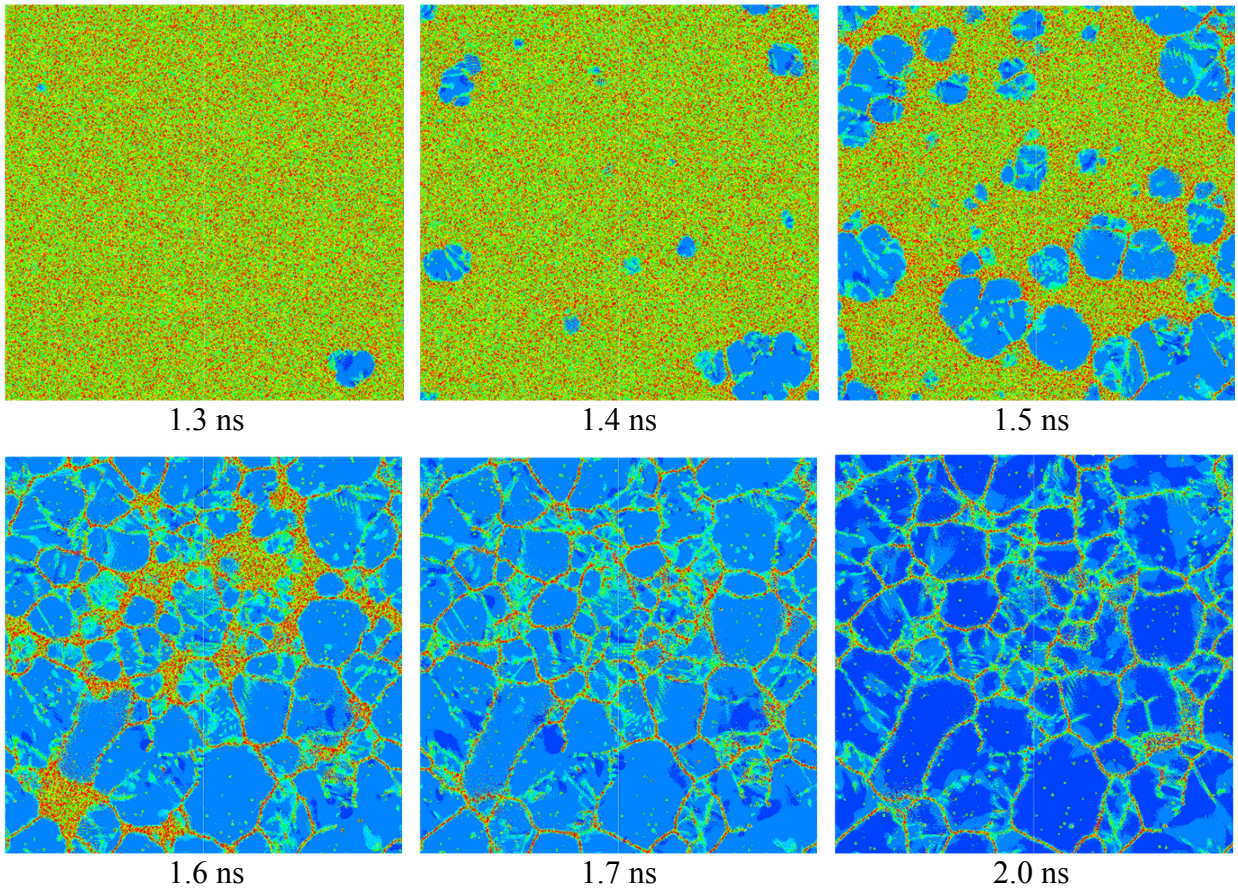

Figure 3: Top view of atomic configurations generated in a TTM-MD simulation of Ag (001) target irradiated by a 100 fs laser pulse at an absorbed fluence of 0.085 J/cm^2. The snapshots are shown for the time period when the nucleation of new crystallites in a strongly undercooled surface region leads to the rapid solidification of the surface region. The atoms are then colored by their potential energies, with the same scale used as in Fig. 2. A thin top surface layer is blanked to expose the underlying structure.

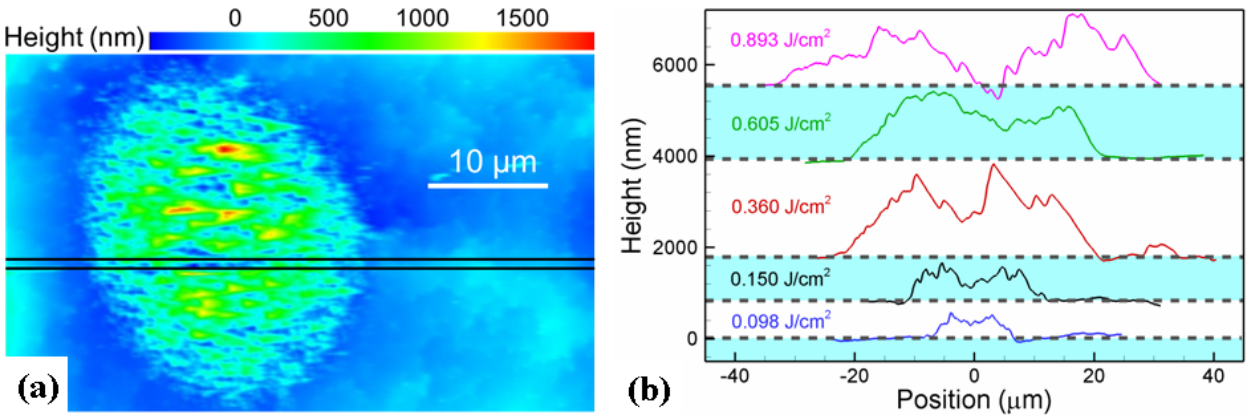

Figure 4: An example of AFM surface scan of a spot on Ag (001) surface irradiated by a 100 fs laser pulse at an absorbed laser fluence of 0.15 J/cm^2 (incident fluence of 4.87±0.08 J/cm^2) with the white scale bar corresponding to 10 μm (a) and AFM line scans of several spots generated by irradiation at absorbed fluences ranging from 0.098 J/cm^2 (incident fluence of 3.17 J/cm^2) to 0.893 J/cm^2 (incident fluence of 28.8 J/cm^2) (b). The black horizontal lines in (a) mark the area from which the average line out is computed and shown for 0.15 J/cm^2 in (b). For clarity, the curves in (b) are offset vertically. Note that the indicated absorbed fluences have been converted from experimentally measured incoming fluences using a reflectivity of 0.969.

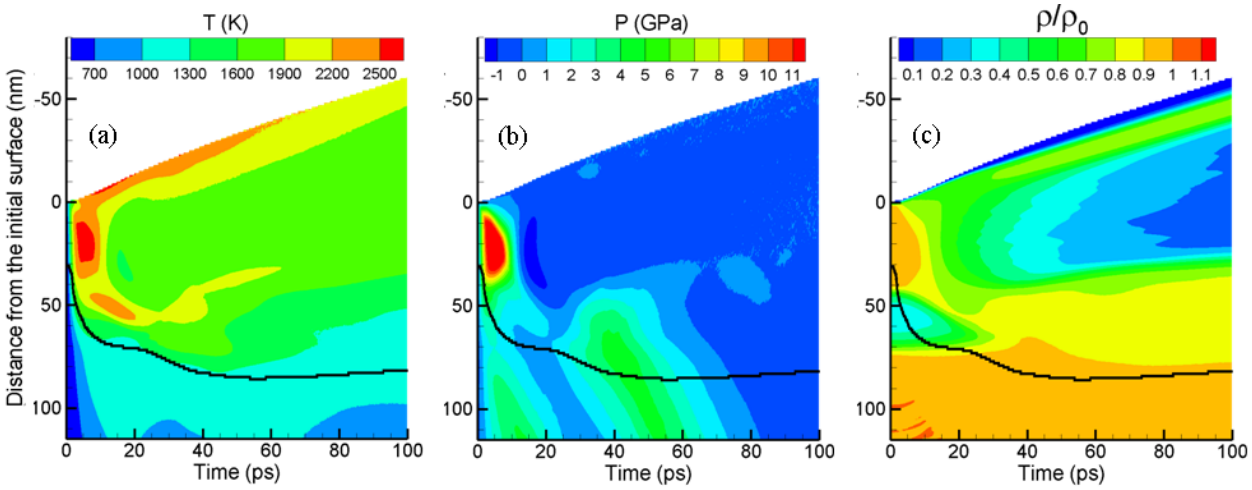

Figure 5: The evolution of thermodynamic parameters in a simulation of a 2nd 100 fs pulse irradiation of a target modified by the first pulse as shown in Figs. 1 - 3. Both pulses deliver the same absorbed laser fluence of 0.085 J/cm^2 and the target is slowly cooled down to 300 K between the pulses. The contour plots show the lattice temperature (a), pressure (b), and density (c) in the top surface region (down to 115 nm below the initial surface) during the first 100 ps after the 2nd pulse irradiation. The density is normalized to the density ρ_0 of Ag at 300 K. The black lines separate the melted region from the crystalline bulk of the target. The surface of the target obtained after 1st laser pulse irradiation is shifted to zero before applying the 2nd laser pulse.

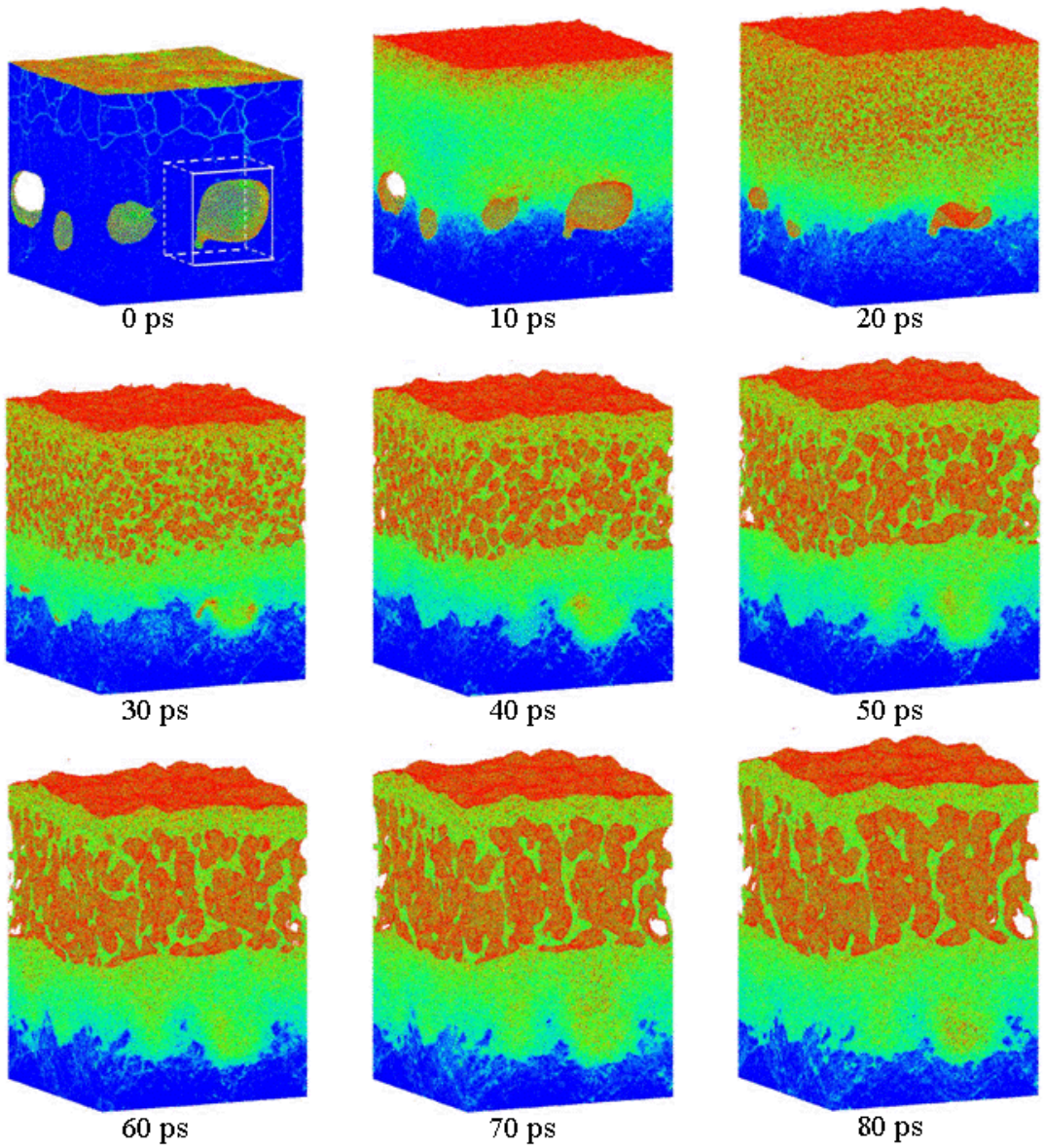

Figure 6: Snapshots of atomic configurations obtained in a simulation of the 2nd 100 fs pulse irradiation of a target modified by the first pulse as shown in Figs. 1 - 3. The snapshots are shown for the initial stage of the spallation process, up to 80 ps after the laser pulse. To reduce thermal noise in atomic positions and energies, the atomic configurations are quenched for 0.2 ps using the velocity dampening technique. The atoms are then colored by their potential energies, with the scale chosen from -2.80 eV (blue) to -2.35 eV (red) to ensure a clear representation of the melting, void collapse, and spallation processes. The white box in the first snapshots outlines the area for which an enlarged view of the collapse of the sub-surface void is shown in Fig. 7. An animated sequence of snapshots from this simulation with a time resolution of 5 ps can be found at Ref. [58].

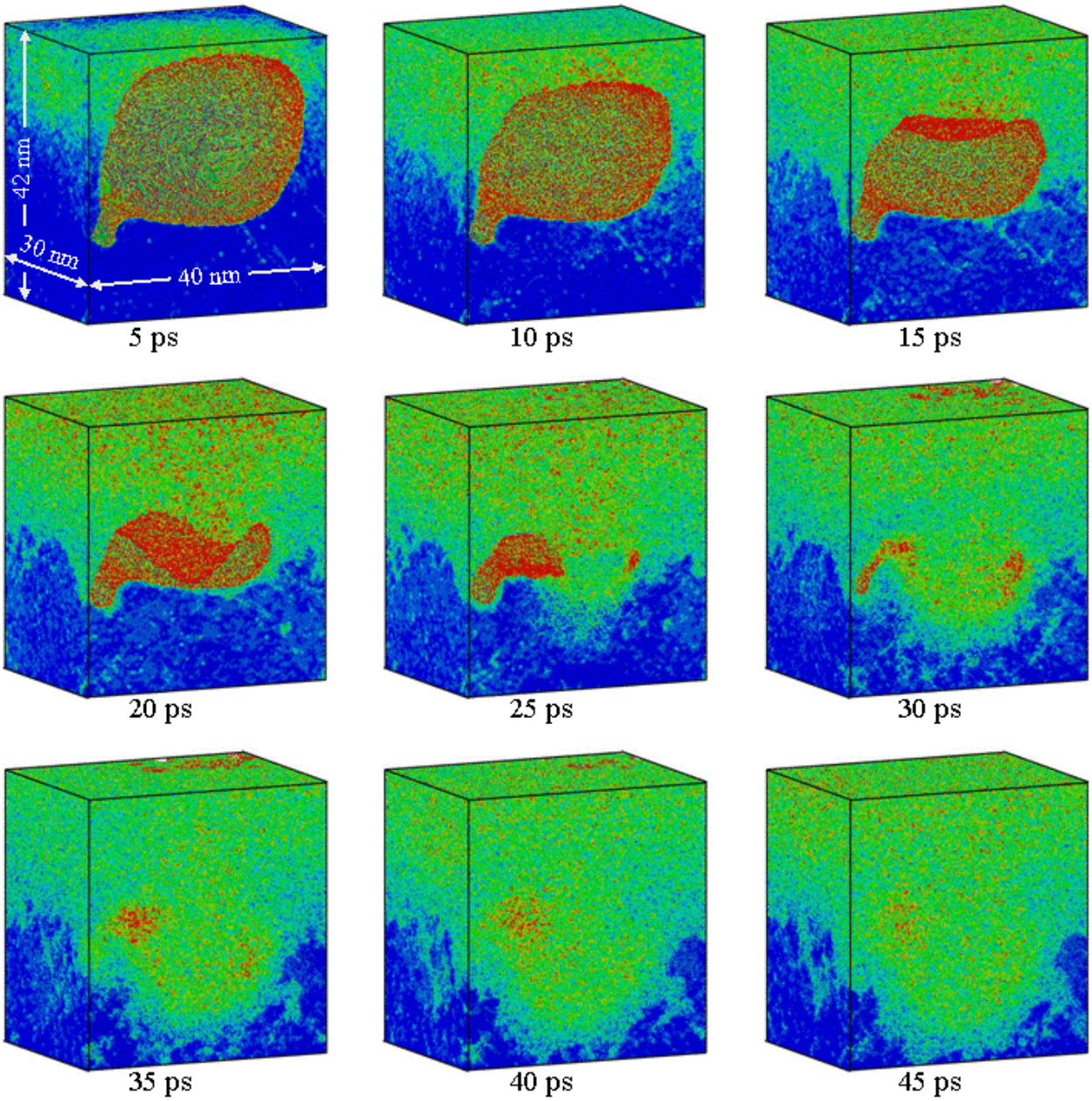

Figure 7: An enlarged view of the collapse of one of the sub-surface voids present in the target prior to the irradiation with the 2nd laser pulse. The region shown in this figure is outlined by a white box in the first snapshot shown in Fig. 6. An animated sequence of snapshots showing the evolution of this area of the system can be found at Ref. [58].

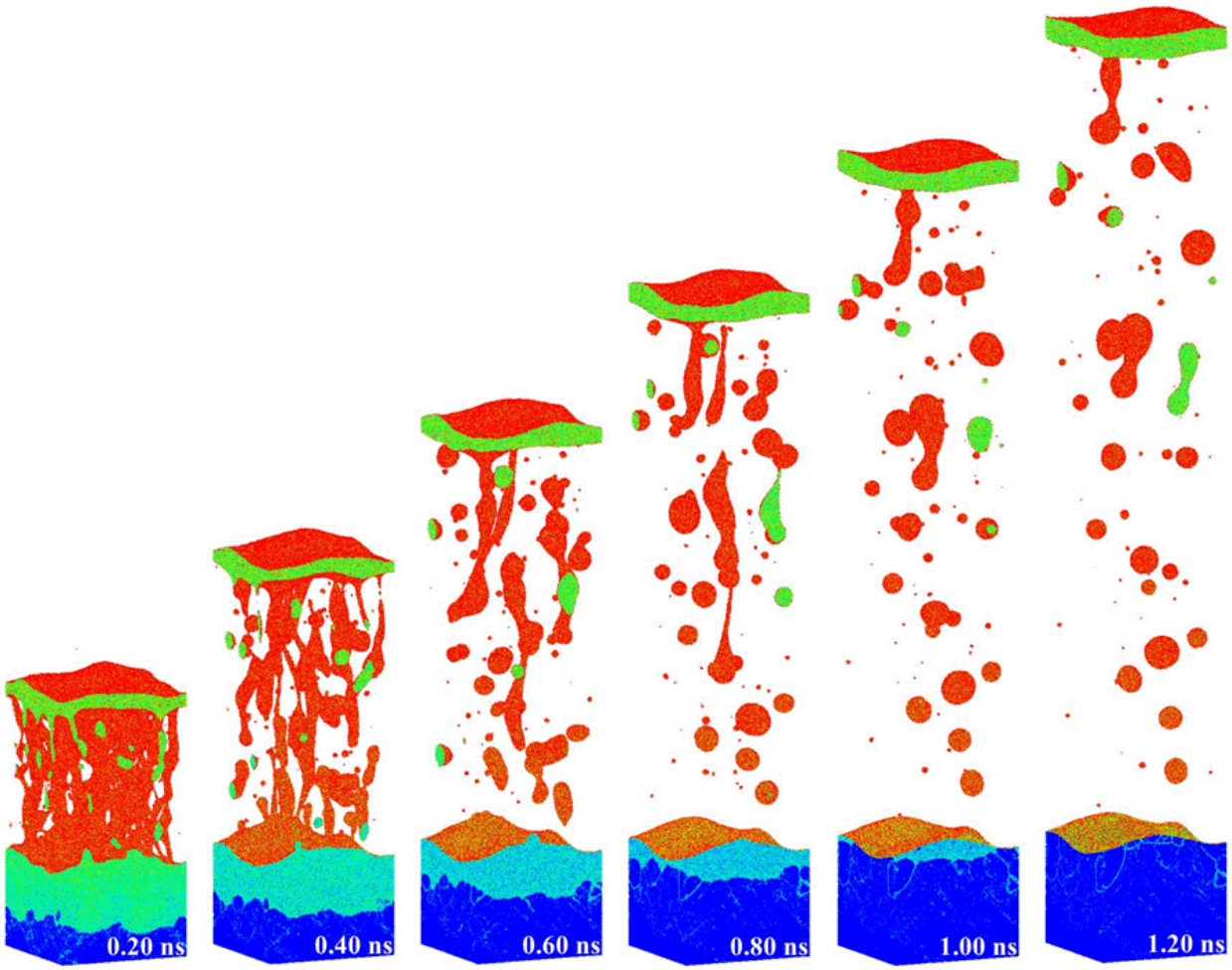

Figure 8: Same as Fig. 6, but for a longer time period from 200 ps to 1200 ps. The scale of potential energies used for coloring of the atoms, from -2.84 eV (blue) to -2.65 eV (red) is different from Fig. 6 and is chosen to ensure a clear representation of the spallation and resolidification processes. An animated sequence of snapshots from this simulation with time resolution of 50 ps can be found at Ref. [58].

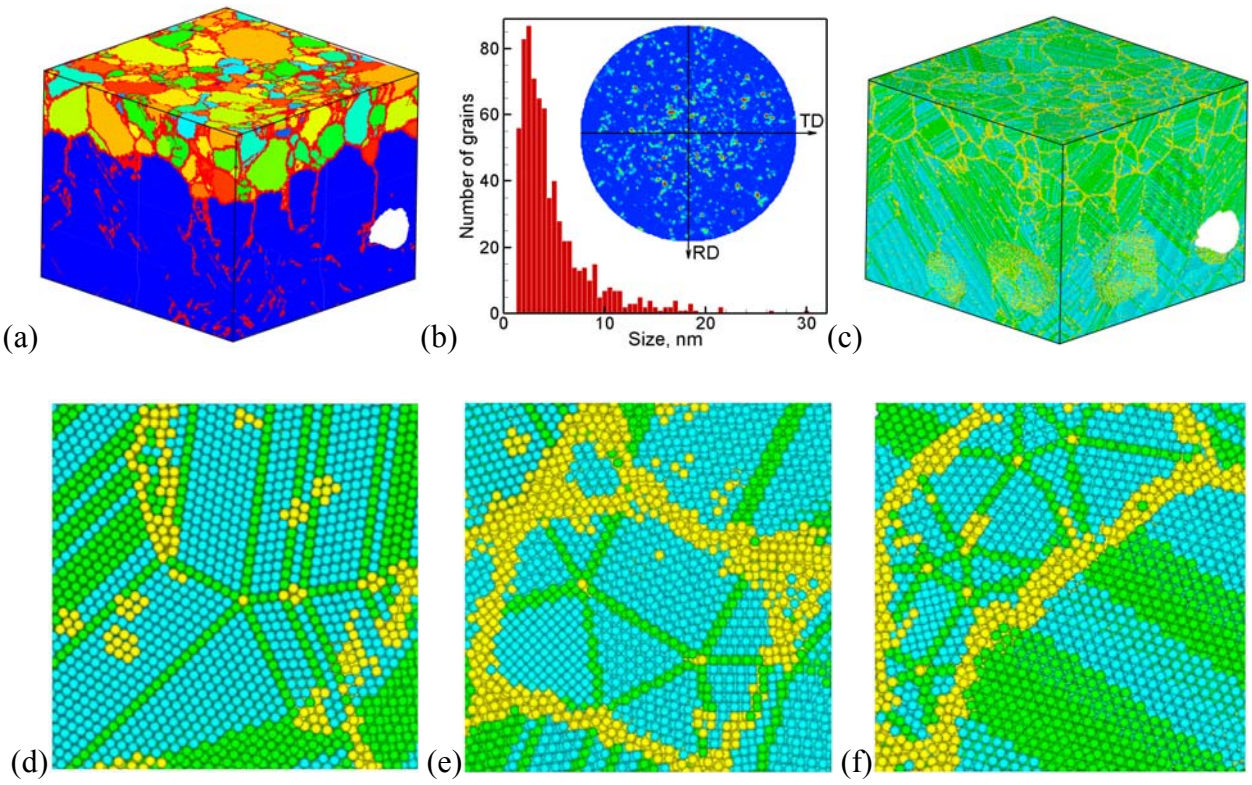

Figure 9: Snapshots and the results of structural analysis of the final atomic configuration generated by 2 ns after the laser pulse in the simulation illustrated in Figs. 1 - 3. In (a), the atoms are colored by the smallest angle between the [001] direction of the original fcc lattice and a <111> direction in the corresponding grain. The blue bottom part of the snapshot is the region that experienced epitaxial resolidification and the red atoms belong to the grain boundaries. In (b), the nanograin size distribution and <111> pole figure indicating the random orientations of the nanograins are shown. The grain sizes are expressed in units of diameters of spherical grains with equivalent volumes. In (c-f), the atoms are colored by their local structural environment, so that the fcc, hcp, and bcc atoms are colored light blue, green, and blue, respectively, and the yellow atoms belong to grain boundaries and other crystal defects. With this coloring scheme, a single and a double green layers on a light blue background correspond to a twin boundary and a stacking fault in the fcc structure. The surface atoms in (c) are blanked to expose the underlying defect structure. The images in (d-f) show enlarged views of three representative elements of nanostructure obtained by making an in-plane (parallel to the surface) cross-section of the top part of the target.